Applied Physics Letters

Local ordering in Ge/Ge–Sn semiconductor alloy core/shell nanowires revealed by extended x-ray absorption fine structure (EXAFS)

Cite as: Appl. Phys. Lett. **122**, 062103 (2023); https://doi.org/10.1063/5.0136746
Submitted: 28 November 2022 • Accepted: 22 January 2023 • Published Online: 07 February 2023

J. Zach Lentz, J. C. Woicik, Matthew Bergschneider, et al.

AIP Publishing

Applied Physics Letters ARTICLE scitation.org/journal/apl

Local ordering in Ge/Ge–Sn semiconductor alloy core/shell nanowires revealed by extended x-ray absorption fine structure (EXAFS)

Cite as: Appl. Phys. Lett. **122**, 062103 (2023); doi: 10.1063/5.0136746
Submitted: 28 November 2022 · Accepted: 22 January 2023 ·
Published Online: 7 February 2023

J. Zach Lentz,[1] J. C. Woicik,[2] Matthew Bergschneider,[3] Ryan Davis,[4] Apurva Mehta,[5] Kyeongjae Cho,[3] and Paul C. McIntyre[1,4,a)]

AFFILIATIONS

[1]Department of Materials Science and Engineering, Stanford University, Stanford, California 94305, USA
[2]Materials Measurement Science Division, Material Measurement Laboratory, National Institute of Standards and Technology, Gaithersburg, Maryland 20899, USA
[3]Department of Materials Science and Engineering, University of Texas at Dallas, Richardson, Texas 75080, USA
[4]Stanford Synchrotron Radiation Lightsource (SSRL), SLAC National Accelerator Laboratory, Menlo Park, California 94025, USA
[5]Linac Coherent Lightsource (LCLS), SLAC National Accelerator Laboratory, Menlo Park, California 94205, USA

[a)]**Author to whom correspondence should be addressed:** pcm1@slac.stanford.edu

ABSTRACT

Short-range atomic order in semiconductor alloys is a relatively unexplored topic that may promote design of new materials with unexpected properties. Here, local atomic ordering is investigated in Ge–Sn alloys, a group-IV system that is attractive for its enhanced optoelectronic properties achievable via a direct gap for Sn concentrations exceeding ≈10 at. %. The substantial misfit strain imposed on Ge–Sn thin films during growth on bulk Si or Ge substrates can induce defect formation; however, misfit strain can be accommodated by growing Ge–Sn alloy films on Ge nanowires, which effectively act as elastically compliant substrates. In this work, Ge core/$Ge_{1-x}Sn_x$ ($x \approx 0.1$) shell nanowires were characterized with extended x-ray absorption fine structure (EXAFS) to elucidate their local atomic environment. Simultaneous fitting of high-quality EXAFS data collected at both the Ge *K*-edge and the Sn *K*-edge reveals a large (≈ 40%) deficiency of Sn in the first coordination shell around a Sn atom relative to a random alloy, thereby providing the first direct experimental evidence of significant short-range order in this semiconductor alloy system. Comparison of path length data from the EXAFS measurements with density functional theory simulations provides alloy atomic structures consistent with this conclusion.

Short-range order (SRO) in solid solutions has been shown to contribute to its mechanical properties,[1–4] but its presence and resulting effects on the electronic behavior of semiconductor alloys have not been widely studied. This prompts interest in determining the degree of SRO in semiconductor alloys. Ge–Sn solid solutions have garnered much interest recently,[5–12] primarily for their capability to achieve a tunable direct bandgap in a group IV semiconductor system that is compatible with complementary metal oxide semiconductor (CMOS) technology, and for their greater carrier mobility[13] compared to silicon and germanium CMOS transistor channel materials. However, the lattice parameter difference between Ge and diamond cubic α-Sn (≈14%)[14–16] can promote the formation of various types of defects, especially after post-growth annealing, including Sn precipitation.[17–23] The lattice mismatch means that relatively defect-free epitaxial thin films grown on typical Si or Ge substrates tend to be in a state of biaxial compressive strain, which hinders the transition to a direct gap.[24] For these reasons, this study focuses on Ge–Sn alloy shells, deposited around Ge nanowires, which are grown by the vapor–liquid–solid (VLS) growth mechanism. The growth process and characteristics of such nanowires have been reported in detail elsewhere.[25–27] This core/shell nanowire geometry is particularly advantageous: the $Ge_{1-x}Sn_x$ shell grows on an effectively elastically compliant substrate and, therefore, can be essentially strain-free for shell thicknesses comparable to or greater than the core diameter.[26,28] In fact, Ge core/$Ge_{1-x}Sn_x$ shell nanowire photodetectors have been shown recently to achieve impressive responsivity and photoconductive gain.[12]

SRO in nanowire structures was investigated via extended x-ray absorption fine structure (EXAFS). EXAFS has been used previously to study changes in bond lengths, often as a function of composition, in several semiconductor systems[29–32] as well as SRO in metallic systems.[4] There have recently been a few studies of SRO in Ge–Sn using atom probe tomography (APT). Assali *et al.*[33] found no SRO in their Ge–Sn films, even in analysis of the correlation of nearest neighbor distributions. This could be due to the high residual strain in their films, which another analysis found affected the degree of SRO.[34] Liu *et al.*[34] performed a detailed APT study of SRO in Ge–Sn alloy thin films and found a small degree of Sn–Sn correlation, which depended on depth beneath the sample surface and strain in the film, but not on the average alloy composition. In contrast, computational work on the local atomic structure of Ge–Sn alloys indicates a much higher degree of SRO, wherein the shell of first nearest neighbors around Sn is nearly devoid of Sn, with the redistribution of these Sn atoms to the third shell.[35]

There has been one published report to date on EXAFS of crystalline Ge–Sn alloys.[36] However, the data were collected at the Sn *K*-edge only and were limited to a narrow k-range. Also, the presence of localized amorphous regions of $Ge_{1-x}Sn_x$ material limited that analysis. Furthermore, this study was focused on point defects in Ge–Sn alloys, rather than SRO.

Figure 1 provides details of the sample examined in this study. The inset shows a scanning electron microscopy (SEM) image of the as-grown sample. The image demonstrates that the $Ge_{1-x}Sn_x$ shells have sharp facets indicative of high crystalline quality with no visible Sn precipitation.[37] Previously reported transmission electron microscopy (TEM) images indicate that the entirety of the core/shell nanowires is single crystalline.[25] Figure 1 also shows a symmetric 2θ-ω x-ray diffraction (XRD) scan of the sample near the (333) peak.

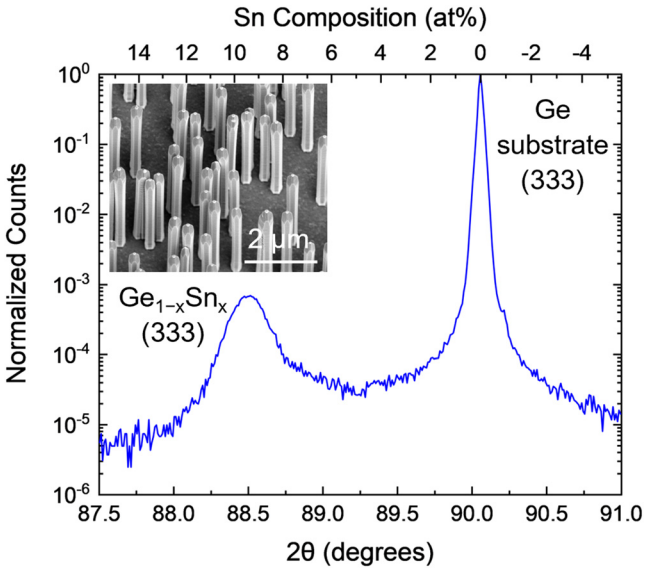

FIG. 1. XRD symmetric 2θ-ω scan of Ge/$Ge_{1-x}Sn_x$ core/shell nanowires. Top axis shows Sn composition corresponding to the diffraction angle, assuming an unstrained Ge–Sn alloy and applying Vegard's law. Inset: scanning electron microscopy image of Ge/$Ge_{1-x}Sn_x$ core/shell nanowires at 30° of stage tilt.

The peak at ≈90.5° is from the single crystal Ge(111) substrate, and the peak at ≈88.5° is from the $Ge_{1-x}Sn_x$ shell material. Vegard's law may be used to estimate the Sn content of the $Ge_{1-x}Sn_x$ material, and since, based on the previous work,[28,38] the $Ge_{1-x}Sn_x$ is unstrained for the shell thickness (≈ 110 nm) and core diameter (≈ 50 nm) here, this makes the Bragg angle of its peak a direct reflection of its Sn composition, leading to the composition axis at the top of Fig. 1. The center of the $Ge_{1-x}Sn_x$ peak corresponds to a composition of ≈9.4 at. % Sn. Previous XRD-estimated compositions of $Ge_{1-x}Sn_x$ shells deposited in this CVD process have been validated by energy-dispersive x-ray spectroscopy (EDS) composition measurements during scanning transmission electron microscopy (STEM) imaging of core/shell nanowires and nanowire cross sections.[25,26]

EXAFS samples were prepared by exfoliating the nanowires from their growth substrate using tape. Data were collected at beamline 11–2 at the Stanford Synchrotron Radiation Lightsource (SSRL). The sample was loaded in a liquid He cryostat, and both the Ge *K* and Sn *K* absorption edge data were collected in fluorescence. The Ge *K*-edge fluorescence was collected using a passivated implanted planar silicon (PIPS) detector, while the Sn *K*-edge fluorescence was collected using a monolithic 100-element Ge detector. Soller slits were placed in front of each detector, as well as a Ga filter for the Ge *K*-edge and a Cd filter for the Sn *K*-edge, to enhance the signal-to-background ratio.

Raw EXAFS data were reduced using SIXPACK,[39,53] and background subtraction and fitting were performed using ATHENA and ARTEMIS,[40,53] respectively. The data were fit to the EXAFS equation, which is Eq. (S1). The Ge *K*-edge data were Fourier transformed using the range $k = 30$–$190\,\mathrm{nm}^{-1}$, and the Sn *K*-edge data were Fourier transformed using the range $k = 30$–$195\,\mathrm{nm}^{-1}$; a Hanning window with $dk = 1\,\mathrm{nm}^{-1}$ was used for both edges. The Fourier transforms of the k^2-weighted data were then fit in *R* space for both edges over the range of $R = 0.15$–0.47 nm, corresponding to the first three coordination shells around the absorbing atom. The two datasets were fitted simultaneously using nine distinct single-scattering paths for the first three coordination shells (calculated by FEFF[41,53]) each consisting of Ge(absorber)-Ge(scatterer), Ge(absorber)-Sn(scatterer), Sn(absorber)-Ge(scatterer), and Sn(absorber)-Sn(scatterer). Paths for each coordination shell with Ge(absorber)-Sn(scatterer) were fit with the same ΔR and σ^2 parameters as paths with Sn(absorber)-Ge(scatterer). The composition *x* of the alloy was incorporated (and fit) by multiplying the coordination number for the path by *x* for a path with Sn scatterer or by $1 - x$ for a path with Ge scatterer. Therefore, the fit included 23 parameters: amplitude reduction factor (S_0^2) for both edges; energy shift (ΔE_0) for both edges; nine changes in path length (ΔR) and Debye–Waller factor (σ^2) for the nine paths; and composition *x*. It should be noted that this fitting model represents the simplest physical EXAFS model for a random binary alloy with two absorbing atoms and three coordination shells.

Figure 2 shows the "raw" (unfiltered) k^2-weighted $\chi(k)$ EXAFS data and fits for (a) the Ge *K*-edge data and (b) the Sn *K*-edge data. It is important at the outset to note the excellent quality of these data. Such high-quality data extending to $k = 200\,\mathrm{nm}^{-1}$ were obtained by the combination of several factors. First, using a liquid He cryostat was essential to reduce thermal vibration damping of the EXAFS. Even more importantly, as the sample is not a conventional thin film, it was possible to remove the newly grown nanowire material from the substrate by using tape, thereby eliminating the need for a grazing

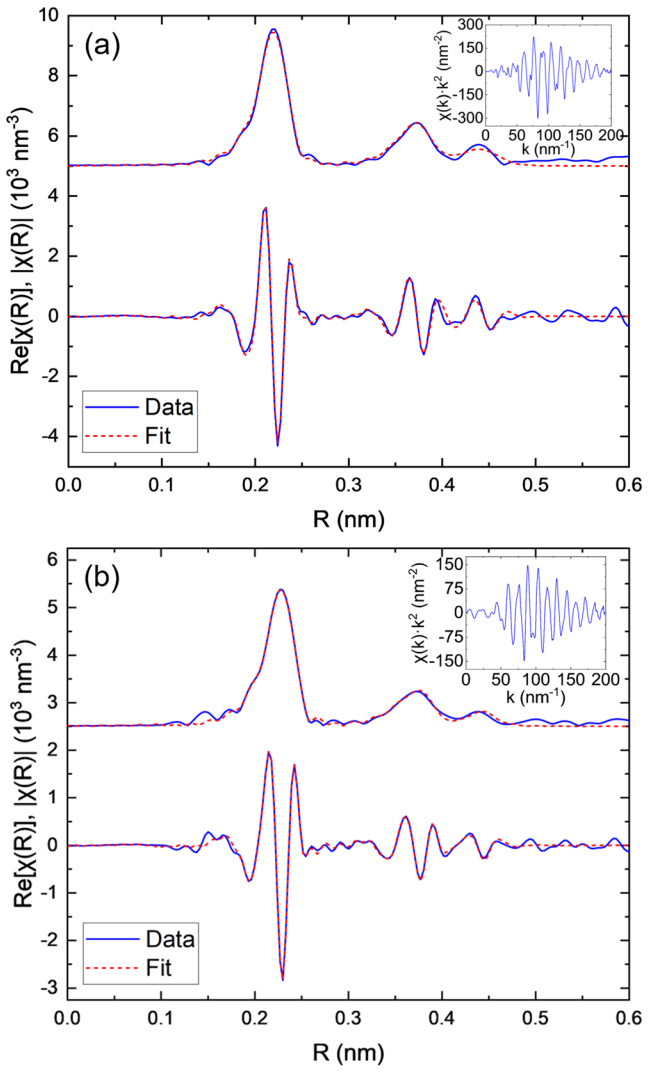

FIG. 2. Fits to the Fourier transforms of (a) Ge *K*-edge and (b) Sn *K*-edge data of the sample. The top curves are the data and fit of the magnitude of the Fourier transform of the EXAFS, |X(R)|, and the bottom curves are those of the real part of the Fourier transform of the EXAFS, Re[X(R)]. Insets: raw k^2-weighted $\chi(k)$ data.

incidence EXAFS geometry and contamination of the signal due to the substrate's absorption as well as Bragg peaks from the substrate or layer itself.[42]

Both fits closely follow the data. It should be noted that the Ge *K*-edge data will include signal from the pure Ge core in addition to the $Ge_{1-x}Sn_x$ shell, but the core constitutes less than 4% of each nanowire's volume. In addition, a coherent interface between the core and shell is expected with the core strained to match the lattice parameter of the shell, while the shell remains strain-free.[26,28] Therefore, the Ge core should be only a minor perturbation to the analysis, as supported by the close agreement of the EXAFS ($x = 0.11 \pm 0.02$) and XRD ($x \approx 0.094$) determinations of the alloy composition.

Figure 3 shows the results of the fitted Debye–Waller factors (σ^2) for the first three coordination shells. Clearly, the Sn–Sn scattering paths

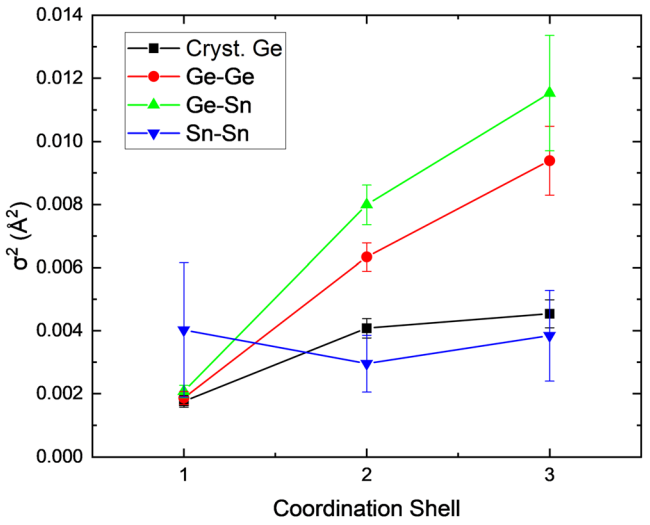

FIG. 3. Fitted values of Debye–Waller factors (σ^2) for the random-alloy model. The plot also includes EXAFS fitting results for a pure crystalline Ge sample recorded in the same liquid He cryostat.

reveal anomalous values compared to the others, despite the EXAFS determination of *x* being equivalent to that determined by XRD.

To shed light on the Sn–Sn Debye–Waller factors, Fig. 4 shows chemically specific sums of the fitted single-scattering paths. That is, panel (a) shows the sum of paths with Ge(absorber)-Ge(scatterer); panel (b) with Ge(absorber)-Sn(scatterer); panel (c) with Sn(absorber)-Ge(scatterer); and panel (d) with Sn(absorber)-Sn(scatterer). The fitted intensity for Sn atoms in the first shell around another Sn atom is much lower relative to its second and third shells compared to the other types of paths. Because of the correlation between coordination number and Debye–Waller factor in an EXAFS fitting model, these results taken together indicate that the first shell around an absorbing Sn atom is significantly devoid of Sn, while the second and third shells appear Sn rich, consistent with the results of the theoretical prediction of SRO in Ge–Sn.[35]

The dramatic reduction in intensity of the first Sn–Sn scattering path was quantified using an additional multiplicative parameter *s* (referred to as the "swap parameter"). The addition of *s* to the fit reduced the Sn–Sn first shell Debye–Waller factor significantly to a value consistent with the values for Ge–Ge and Ge–Sn and produced a value of $s = 1.7 \pm 1.2$, indicating a reduction in the number of Sn atoms in the first shell around another Sn atom by ≈40% compared to what would be expected for a random alloy. (The large error bar is due to the high correlation between *s* and σ^2.) The Sn–Ge coordination was then also adjusted by the opposite amount (to maintain a coordination number of four around the absorbing Sn atom), and, indeed, the fit was again improved, but not significantly over the model that ignored this correction. Redistribution of Sn to both the second and third shells in the model was also attempted, and again the fits did not show significant improvement, regardless of the relative fraction of additional Sn in these shells. This result is consistent with the fact that the redistribution of Sn to the second and third shells is only a minor perturbation to their total coordination because the coordination number of the second and third shells is 12, whereas that of the first

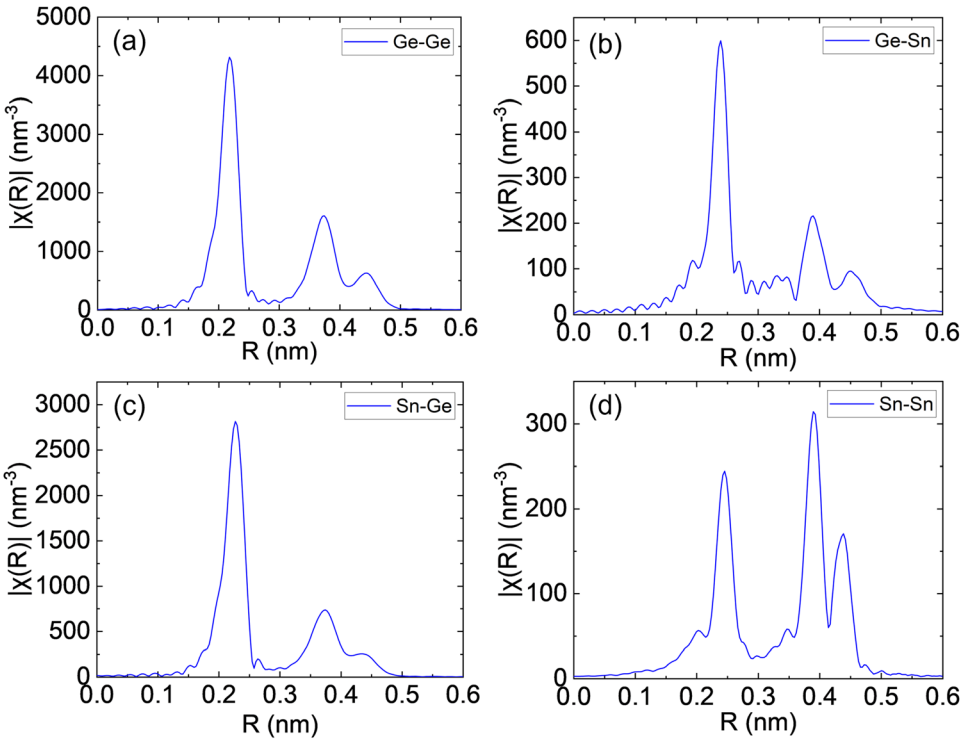

FIG. 4. Sums of fitted single-scattering paths. The first atom in the legend is the absorber and the second is the scatterer.

shell is four. Consequently, no additional quantitative information could be gleaned other than that the first shell around a Sn atom is deficient in Sn, and that this Sn is moving to the second and third shells.

The value of the swap parameter indicates much stronger local ordering than that detected in published reports using APT, corresponding to a short-range order parameter of 0.59 ± 0.42, whereas Liu *et al.* obtained 0.85–1.15.[34] Liu *et al.* suggested that the modest SRO measured in their experiments compared to theory[35] may be a consequence of the non-equilibrium nature of Ge–Sn alloys, which have been grown at low temperature to enable Sn incorporation above the solid solubility limit. The growth temperature of the films described in Ref. 34 was not reported. However, in Ref. 33, which similarly detected much less SRO than the present EXAFS study, the authors employed temperatures of 320, 300, and 280 °C during Ge–Sn growth, all of which are higher compared to the Ge-Sn shell growth temperature of 275 °C employed herein. Therefore, the present results do not seem consistent with the suggestion by Liu *et al.* that Ge–Sn films grown at lower temperatures should show less SRO. Another factor that could be influencing the amount of SRO in these samples is the film growth rate. Assali *et al.*[33] obtained growth rates of roughly 3, 2.4, and 1.3 nm/min for layers having reported compositions of 7 at. % Sn, 12 at. % Sn, and 17 at. % Sn, respectively. All of these film growth rates are greater than the growth rate of the 9.4 at. % Sn nanowire shells reported herein, which is about 1 nm/min. This slower shell growth rate may promote local Sn redistribution during atom incorporation into the shell, facilitating SRO.

The values emerging from the fits, both with and without the swap parameter, are shown in Table S1, and further discussion of them is warranted. Amplitude reduction factors (S_0^2) of 1 are obtained for both edges, which are the same values obtained for pure Ge and pure Sn reference samples measured at the same beamline (see supplementary material). This suggests that the first three shells are fully occupied within the accuracy of these measurements, contrary to the results of Gencarelli *et al.*,[36] which showed unusually low coordination numbers in the second and third shells. Additionally, it should be noted that the fitted value of composition, both with and without the swap parameter *s*, corresponds to that obtained from XRD, adding credence to the robustness of the fit.

The alloy path length results are also of interest and are shown in Fig. 5(a) as relative strain of those path lengths, for the first three coordination shells, where the relative strain is defined as

$$\frac{\Delta R}{R} = \frac{R_{measured} - R}{R}, \tag{1}$$

where R_{measured} is the measured path length from the fit to the EXAFS data and R is the corresponding path length in room temperature crystalline Ge. To facilitate interpretation of these results, first principles simulations were performed using the Vienna *Ab-initio* Simulation Package (VASP).[43,53] The spin-polarized calculations were completed with the revised Perdew–Berke–Ernzerhof generalized gradient approximation[44] for exchange-correlation interactions, with plane wave basis cutoff energy of 8.33×10^{-18} J (520 eV) and augmented-wave pseudopotentials.[45,46] Ionic relaxation was completed with gamma-centered reciprocal-space grid with a minimum spacing of 0.003 nm^{-1}, and the supercell volume fixed to the desired volumetric strain. The supercell was formed from a $2 \times 2 \times 2$ grid of unit cells, with three of eight being identical cells containing two Sn atoms (to

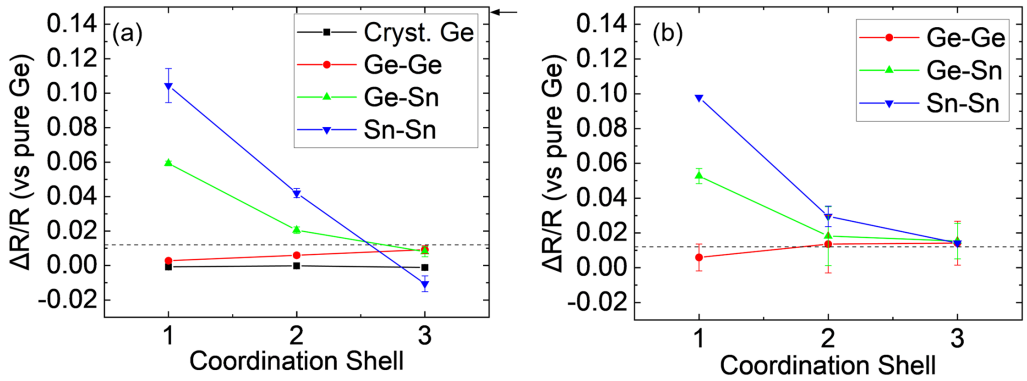

FIG. 5. EXAFS-measured relative strain $\Delta R/R$ in each path for the random-alloy model (no swap parameter) (a) and calculated $\Delta R/R$ (b). The horizontal dashed line corresponds to the strain determined from the XRD alloy peak (Fig. 1). Panel (a) also includes EXAFS fitting results for a pure crystalline Ge sample recorded in the same liquid He cryostat. The arrow at the top right of (a) corresponds to the path lengths of pure diamond cubic Sn ($\Delta R/R = 0.147$).

match the composition of the experimental sample). The Sn atoms were configured as either first nearest neighbors (1NN), second nearest neighbors (2NN), or third nearest neighbors (3NN). Simulations were performed for three different supercells: one containing the 1NN configuration, another the 2NN configuration, and the last the 3NN configuration. It is notable that relative energies indicate similar energies for the 2NN and 3NN configurations, while the 1NN configuration has substantially higher energy (Table S2), supporting experimental results herein and the aforementioned theoretical results.[35] The supercell volume was expanded by 1.3% relative to pure Ge in each axis, to correspond to the sample's lattice parameter measured by XRD (Fig. 1), and then fixed. All 64 atoms were allowed to relax within the constrained volume supercell, and path lengths were tabulated for equivalent configurations of atom pairs (i.e., Ge and 1NN Ge, Ge and 1NN Sn, etc.) out to the third coordination shell. Such path lengths were averaged over the value from the three independent simulations with equal weight, except for the Sn–Sn paths, where each of the three data points comes from a separate simulation. Figure 5 compares the theoretical $\Delta R/R$ values [Fig. 5(b)] with the experimental values [Fig. 5(a)] determined by EXAFS. Trends match the EXAFS measured strain, with the notable exception of the absolute values of the second and third shell Sn–Sn strain, which will be expanded on below.

Based on the seminal EXAFS study of III–V semiconductors by Mikkelsen and Boyce,[47] significant bond length differences in the Ge–Sn alloy system should be expected relative to the bond lengths in pure Ge and pure Sn. Mikkelsen and Boyce determined that the bond lengths in the zinc blende III–V alloy $Ga_{1-x}In_xAs$ do not follow the simple virtual-crystal approximation (VCA), but rather the In–As and Ga–As bond lengths maintain their own chemically distinct values, and these values vary linearly as a function of alloy composition x by $\approx 1/4$ of the natural bond length difference between them. For the case of the true binary alloy Si–Ge system, both experimental[48–50] and theoretical work[51] have found similar results. Clearly, significant differences between the Sn–Sn and Ge–Ge bond lengths are observed in this work, in both theory and experiment, with the Ge–Sn bond length being close to the average of the two. It is also clear that with increasing shell distance, all distances tend to their natural VCA average,[52] although the Sn–Sn 3NN distance as determined by EXAFS is found much closer to the 3NN distance of pure crystalline Ge. This anomaly may be associated with the non-randomness of the alloy that would likely favor smaller third shell Sn–Ge–Ge–Sn distances over larger Sn–Ge–Sn–Sn and Sn–Sn–Sn–Sn distances,[51] together with the apparent expansion of 2NN Sn-Sn distances to accommodate the local strain[53] (for information on the influence of multiple scattering related to this point, see the supplementary material). Assuming the "$1/4\ x$" natural first shell bond length dependence of Mikkelsen and Boyce,[47] the predicted first shell bond lengths would be 0.2454 nm for Ge–Ge, 0.2591 nm for Ge–Sn, and 0.2728 nm for Sn–Sn, for a Ge–Sn alloy of the composition studied here, in satisfactory agreement with the fitting results in Table S1, and nicely supporting the accepted chemical dependence of bond lengths in semiconductor alloy systems.

See the supplementary material for the EXAFS equation, which was used to model the EXAFS data, values of all the parameters emerging from the fit to the EXAFS data, data from the pure material reference samples, information on the simulations of defect energies, and information on the influence of multiple scattering on the Sn-Sn 3NN distance.

This material is based upon work supported by the U.S. Department of Energy, Office of Science, Office of Workforce Development for Teachers and Scientists, Office of Science Graduate Student Research (SCGSR) program. The SCGSR program is administered by the Oak Ridge Institute for Science and Education for the DOE under Contract No. DE-SC0014664.

This research was supported by the U.S. National Science Foundation, Grant No. DMR-2003266.

This research was supported by the U.S. Department of Energy under Award No. DE-SC0023412 and SubAward No. UA2023-351.

Use of the Stanford Synchrotron Radiation Lightsource, SLAC National Accelerator Laboratory, is supported by the U.S. Department of Energy, Office of Science, Office of Basic Energy Sciences under Contract No. DE-AC02-76SF00515.

Part of this work was performed at the Stanford Nano Shared Facilities (SNSF), supported by the National Science Foundation under Award No. ECCS-2026822.

Additional support was provided by the National Institute of Standards and Technology.

The authors acknowledge the Texas Research and Education Cyberinfrastructure Services (TRECIS) Center, NSF Award No. 2019135, and The University of Texas at Dallas for providing HPC resources and support that have contributed to the research results reported within this paper.

M.B. and K.C. are supported by ASCENT, one of the six centers in JUMP, a Semiconductor Research Corporation (SRC) program sponsored by Defense Advanced Research Projects Agency (DARPA).

AUTHOR DECLARATIONS

Conflict of Interest

The authors have no conflicts to disclose.

Author Contributions

John Z. Lentz: Data curation (lead); Formal analysis (equal); Investigation (lead); Methodology (equal); Software (equal); Validation (equal); Visualization (equal); Writing – original draft (lead); Writing – review & editing (equal). **Joseph C. Woicik:** Formal analysis (equal); Methodology (equal); Software (equal); Validation (equal); Visualization (supporting); Writing – original draft (supporting); Writing – review & editing (equal). **Matthew Bergschneider:** Data curation (supporting); Formal analysis (supporting); Investigation (supporting); Methodology (supporting); Software (supporting); Writing – original draft (supporting); Writing – review & editing (equal). **Ryan Davis:** Investigation (supporting); Methodology (supporting); Writing – review & editing (equal). **Apurva Mehta:** Conceptualization (supporting); Methodology (supporting); Supervision (supporting); Validation (supporting); Writing – review & editing (equal). **Kyeongjae Cho:** Conceptualization (supporting); Funding acquisition (supporting); Methodology (supporting); Resources (supporting); Supervision (supporting); Writing – review & editing (equal). **Paul C. McIntyre:** Conceptualization (lead); Funding acquisition (lead); Methodology (equal); Project administration (lead); Resources (lead); Supervision (lead); Validation (equal); Writing – review & editing (equal).

DATA AVAILABILITY

The data that support the findings of this study are available from the corresponding author upon reasonable request.

REFERENCES

[1]R. Zhang, S. Zhao, J. Ding, Y. Chong, T. Jia, C. Ophus, M. Asta, R. O. Ritchie, and A. M. Minor, Nature **581**, 283 (2020).
[2]Y. Wu, F. Zhang, X. Yuan, H. Huang, X. Wen, Y. Wang, M. Zhang, H. Wu, X. Liu, H. Wang, S. Jiang, and Z. Lu, J. Mater. Sci. Technol. **62**, 214 (2021).
[3]R. Zhang, S. Zhao, C. Ophus, Y. Deng, S. J. Vachhani, B. Ozdol, R. Traylor, K. C. Bustillo, J. W. Morris, Jr., D. C. Chrzan, M. Asta, and A. M. Minor, Sci. Adv. **5**, eaax2799 (2019).
[4]F. X. Zhang, S. Zhao, K. Jin, H. Xue, G. Velisa, H. Bei, R. Huang, J. Y. P. Ko, D. C. Pagan, J. C. Neuefeind, W. J. Weber, and Y. Zhang, Phys. Rev. Lett. **118**, 205501 (2017).
[5]R. Kotlyar, U. E. Avci, S. Cea, R. Rios, T. D. Linton, K. J. Kuhn, and I. A. Young, Appl. Phys. Lett. **102**, 113106 (2013).
[6]S. Gupta, Y.-C. Huang, Y. Kim, E. Sanchez, and K. C. Saraswat, IEEE Electron Device Lett. **34**, 831 (2013).
[7]S. Wirths, R. Geiger, N. Von Den Driesch, G. Mussler, T. Stoica, S. Mantl, Z. Ikonic, M. Luysberg, S. Chiussi, J. M. Hartmann, H. Sigg, J. Faist, D. Buca, and D. Grützmacher, Nat. Photonics **9**, 88 (2015).
[8]J. Margetis, S. Al-Kabi, W. Du, W. Dou, Y. Zhou, T. Pham, P. Grant, S. Ghetmiri, A. Mosleh, B. Li, J. Liu, G. Sun, R. Soref, J. Tolle, M. Mortazavi, and S. Q. Yu, ACS Photonics **5**, 827 (2018).
[9]Y. Zhou, W. Dou, W. Du, S. Ojo, H. Tran, S. A. Ghetmiri, J. Liu, G. Sun, R. Soref, J. Margetis, J. Tolle, B. Li, Z. Chen, M. Mortazavi, and S. Q. Yu, ACS Photonics **6**, 1434 (2019).
[10]Y. Zhou, Y. Miao, S. Ojo, H. Tran, G. Abernathy, J. M. Grant, S. Amoah, G. Salamo, W. Du, J. Liu, J. Margetis, J. Tolle, Y. Zhang, G. Sun, R. A. Soref, B. Li, and S.-Q. Yu, Optica **7**, 924 (2020).
[11]E. Talamas Simola, V. Kiyek, A. Ballabio, V. Schlykow, J. Frigerio, C. Zucchetti, A. De Iacovo, L. Colace, Y. Yamamoto, G. Capellini, D. Grützmacher, D. Buca, and G. Isella, ACS Photonics **8**, 2166 (2021).
[12]S. Singh, S. Mukherjee, S. Mukherjee, S. Assali, L. Luo, S. Das, O. Moutanabbir, and S. K. Ray, Appl. Phys. Lett. **120**, 171110 (2022).
[13]J. D. Sau and M. L. Cohen, Phys. Rev. B **75**, 045208 (2007).
[14]K. P. Homewood and M. A. Lourenço, Nat. Photonics **9**, 78 (2015).
[15]H. Pérez Ladrón de Guevara, A. G. Rodríguez, H. Navarro-Contreras, and M. A. Vidal, Appl. Phys. Lett. **84**, 4532 (2004).
[16]S. Zaima, O. Nakatsuka, N. Taoka, M. Kurosawa, W. Takeuchi, and M. Sakashita, Sci. Technol. Adv. Mater. **16**, 43502 (2015).
[17]H. Li, Y. X. Cui, K. Y. Wu, W. K. Tseng, H. H. Cheng, and H. Chen, Appl. Phys. Lett. **102**, 251907 (2013).
[18]Z. P. Zhang, Y. X. Song, Y. Y. Li, X. Y. Wu, Z. Y. S. Zhu, Y. Han, L. Y. Zhang, H. Huang, and S. M. Wang, AIP Adv. **7**, 105020 (2017).
[19]R. Takase, M. Ishimaru, N. Uchida, T. Maeda, K. Sato, R. R. Lieten, and J. P. Locquet, J. Appl. Phys. **120**, 245304 (2016).
[20]P. Zaumseil, Y. Hou, M. A. Schubert, N. Von Den Driesch, D. Stange, D. Rainko, M. Virgilio, D. Buca, and G. Capellini, APL Mater. **6**, 076108 (2018).
[21]C. M. Comrie, C. B. Mtshali, P. T. Sechogela, N. M. Santos, K. Van Stiphout, R. Loo, W. Vandervorst, and A. Vantomme, J. Appl. Phys. **120**, 145303 (2016).
[22]D. Zhang, Y. Liao, J. Li, T. Wen, L. Jin, X. Wang, and J. Kolodzey, J. Alloys Compd. **684**, 643 (2016).
[23]R. Chen, Y. C. Huang, S. Gupta, A. C. Lin, E. Sanchez, Y. Kim, K. C. Saraswat, T. I. Kamins, and J. S. Harris, J. Cryst. Growth **365**, 29 (2013).
[24]S. Gupta, B. Magyari-Köpe, Y. Nishi, and K. C. Saraswat, J. Appl. Phys. **113**, 073707 (2013).
[25]A. C. Meng, C. S. Fenrich, M. R. Braun, J. P. McVittie, A. F. Marshall, J. S. Harris, and P. C. McIntyre, Nano Lett. **16**, 7521 (2016).
[26]A. C. Meng, M. R. Braun, Y. Wang, C. S. Fenrich, M. Xue, D. R. Diercks, B. P. Gorman, M. I. Richard, A. F. Marshall, W. Cai, J. S. Harris, and P. C. McIntyre, Mater. Today Nano **5**, 100026 (2019).
[27]A. C. Meng, M. R. Braun, Y. Wang, S. Peng, W. Tan, J. Z. Lentz, M. Xue, A. Pakzad, A. F. Marshall, J. S. Harris, W. Cai, and P. C. McIntyre, Mater. Today **40**, 101 (2020).
[28]Y. Wang, A. C. Meng, P. C. McIntyre, and W. Cai, Nanoscale **11**, 21974 (2019).
[29]E. Canova, A. I. Goldman, S. C. Woronick, Y. H. Kao, and L. L. Chang, Phys. Rev. B **31**, 8308 (1985).
[30]J. C. Woicik, C. E. Bouldin, M. I. Bell, J. O. Cross, D. J. Tweet, B. D. Swanson, T. M. Zhang, L. B. Sorenson, C. A. King, J. L. Hoyt, P. Pianetta, and J. F. Gibbons, Phys. Rev. B **43**, 2419 (1991).
[31]Y. Kuwahara, H. Oyanagi, R. Shioda, Y. Takeda, H. Yamaguchi, and M. A. M. Aono, Jpn. J. Appl. Phys., Part 1 **33**, 5631 (1994).
[32]J. Woicik, C. Bouldin, and K. Miyano, Phys. Rev. B **55**, 15386 (1997).
[33]S. Assali, J. Nicolas, S. Mukherjee, A. Dijkstra, and O. Moutanabbir, Appl. Phys. Lett. **112**, 251903 (2018).
[34]S. Liu, A. C. Covian, X. Wang, C. T. Cline, A. Akey, W. Dong, S. Q. Yu, and J. Liu, Small Methods **6**, 2200029 (2022).
[35]B. Cao, S. Chen, X. Jin, J. Liu, and T. Li, ACS Appl. Mater. Interfaces **12**, 57245 (2020).
[36]F. Gencarelli, D. Grandjean, Y. Shimura, B. Vincent, D. Banerjee, A. Vantomme, W. Vandervorst, R. Loo, M. Heyns, and K. Temst, J. Appl. Phys. **117**, 095702 (2015).
[37]A. C. Meng, Y. Wang, M. R. Braun, J. Z. Lentz, S. Peng, H. Cheng, A. F. Marshall, W. Cai, and P. C. McIntyre, Nanoscale **13**, 17547 (2021).
[38]S. M. Webb, Phys. Scr. **2005**, 1011.
[39]B. Ravel and M. Newville, J. Synchrotron Radiat. **12**, 537 (2005).
[40]J. J. Rehr, J. Mustre de Leon, S. I. Zabinsky, and R. C. Albers, J. Am. Chem. Soc. **113**, 5135 (1991).

[41]J. Woicik and K. Miyano, Phys. Rev. B **57**, 14592 (1998).
[42]G. Kresse and J. Hafner, Phys. Rev. B **49**, 14251 (1994).
[43]J. P. Perdew, A. Ruzsinszky, G. I. Csonka, O. A. Vydrov, G. E. Scuseria, L. A. Constantin, X. Zhou, and K. Burke, Phys. Rev. Lett. **100**, 136406 (2008).
[44]G. Kresse and D. Joubert, Phys. Rev. B **59**, 1758 (1999).
[45]G. Kresse and J. Furthmüller, Phys. Rev. B **54**, 11169 (1996).
[46]J. C. Mikkelsen, Jr. and J. B. Boyce, Phys. Rev. Lett. **49**, 1412 (1982).
[47]D. B. Aldrich, R. J. Nemani, and D. E. Sayers, Phys. Rev. B **50**, 15026 (1994).
[48]J. C. Aubry, T. Tyliszczak, and A. P. Hitchcock, Phys. Rev. B **59**, 12872 (1999).
[49]I. Yonenaga and M. Sakurai, Phys. Rev. B **64**, 113206 (2001).
[50]N. Mousseau and M. F. Thorpe, Phys. Rev. B **46**, 15887 (1992).
[51]J. C. Woicik, J. Appl. Phys. **112**, 113515 (2012).
[52]Y. Shimura, T. Asano, T. Yamaha, M. Fukuda, W. Takeuchi, O. Nakatsuka, and S. Zaima, Mater. Sci. Semicond. Process. **70**, 133 (2017).
[53]Reference to specific software packages is only for completeness, and it does not represent an endorsement by NIST or the Federal Government of the USA.